Reduction of AC Winding Losses Due to Fringing-Field Effects in High-Frequency Inductors With Orthogonal Air Gaps

Satyaki Mukherjee, *Student Member, IEEE*, Yucheng Gao, *Student Member, IEEE*, and Dragan Maksimović, *Fellow, IEEE*

***Abstract*—In high-frequency inductors, ac winding losses are affected by skin and proximity effects, including uneven current distribution due to fringing magnetic fields around air gaps. It is well known that fringing effects can be mitigated using distributed air gaps. This article is focused on an orthogonal air-gap approach, which is a distributed air-gap technique where gaps are placed in core segments parallel with the windings and in core segments perpendicular to the windings. The orthogonal air-gap approach is developed using a one-dimensional analytical framework and validated by two-dimensional and three-dimensional finite-element simulations. Analytical guidelines are presented to optimize the air-gap distribution to achieve minimum ac resistance. As a case study, a planar inductor is designed for an 8-kW SiC-based buck converter operating at 250 kHz. It is shown how the orthogonal air gaps result in approximately 50% reduction in ac resistance and substantially reduced inductor losses compared to the design using standard air gaps. Experimental validation includes measurements of losses on the converter prototype as well as quality factor measurements in a resonant-circuit test setup.**

***Index Terms*—AC inductor losses, distributed air gaps, fringing effects, high-frequency inductors, inductor ac loss minimization, planar inductors.**

I. Introduction

AC LOSSES, including core losses and winding losses due to skin and proximity effects, limit the performance of inductors in high-frequency power electronics [1]–[4]. In addition, magnetic structures with air gaps lead to higher ac resistance and higher ac winding losses because of uneven current distribution due to fringing magnetic fields around the air gaps [5]–[8]. Many prior works have been focused on mitigating the fringing effects. One approach is to eliminate the air gaps by making use of low permeability materials in the magnetic flux path [8], [9]. Another popular approach consists of distributing the air gaps along the magnetic path, usually in segments of the core parallel with the windings [5]–[7], [10], [11]. It should be noted that machining ferrites in order to introduce additional air gaps may lead to increased core losses [12]–[15]. Shaping the inductor windings away from the gaps has also been proposed as an approach to mitigate the fringing-field effects [16]–[18].

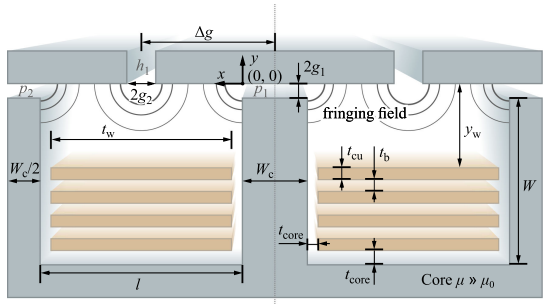

Fig. 1. Planar inductor structure with orthogonal air gaps, including standard perpendicular air gaps p and parallel air gaps h.

This article is focused on a distributed air-gap approach with orthogonally placed air gaps [19], comprising standard air gaps in core segments perpendicular to the windings and air gaps in core segments parallel with the windings, as illustrated by the planar inductor structure in Fig. 1 using an EI core. In this example, in a standard distributed-gap approach, one or more gaps would be placed in the I segment of the core [5]. In the orthogonal-gap approach, gaps are also added between existing E and I segments using a shim, without the need to perform any further machining of the standard core segments. Similar to the conventionally gapped structure, placing the shim adds to the mechanical stability of the orthogonally gapped inductor structure, while the number of core segments remains the same. The orthogonal-gap approach can therefore be considered a distributed-gap approach with a more favorable tradeoff between manufacturing complexity, additional core loss due to machining stress on the ferrite, and winding loss performance of the high-frequency inductor. Furthermore, the approach is particularly well suited for low-profile planar geometries, where the windings cannot be easily placed sufficiently away from the air gaps, as required by the design guidelines provided in [7], [18], [20], and [21].

Manuscript received March 31, 2020; revised May 25, 2020; accepted June 11, 2020. Date of publication June 14, 2020; date of current version September 4, 2020. This work was supported in part by the U.S. Department of Energy (DOE), Office of Energy Efficiency and Renewable Energy, Solar Energy Technologies Office, under Grant DE-EE0008346 and in part by the Advanced Research Projects Agency-Energy (ARPA-E), U.S. Department of Energy under Award DE-AR0000897 in the CIRCUITS program monitored by Dr. Isik Kizilyalli. Recommended for publication by Associate Editor K. Ngo. *(Corresponding author: Satyaki Mukherjee.)*

The authors are with the Department of Electrical Computer and Energy Engineering, University of Colorado, Boulder, CO 80309 USA (e-mail: satyaki.mukherjee@colorado.edu; yucheng.gao@colorado.edu; maksimov@colorado.edu).

Color versions of one or more of the figures in this article are available online at https://ieeexplore.ieee.org.

Digital Object Identifier 10.1109/TPEL.2020.3002507

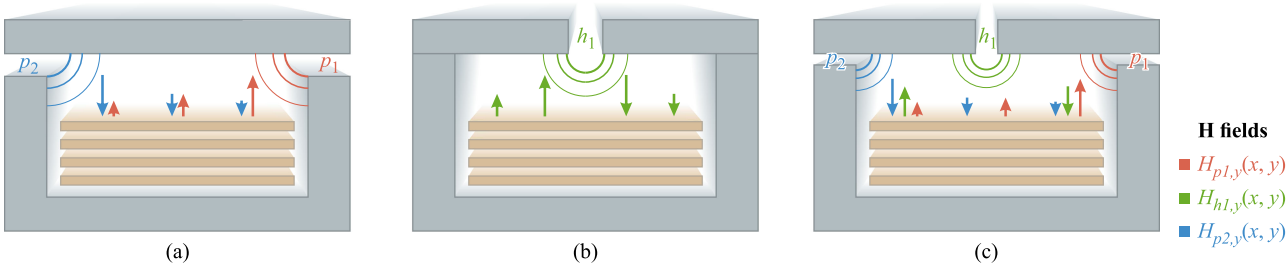

Fig. 2. Effective fringing H-fields in a planar EI inductor structure with (a) conventional (perpendicular) air gaps p, (b) parallel air gaps h, and (c) orthogonal air gaps p and h.

A scalar potential-based one-dimensional (1-D) analytical approach described in [22] and [23] is used to develop an intuitive analytical understanding of how the orthogonal air gaps result in a more uniform current distribution and a reduction in ac resistance. Furthermore, the analytical approach allows for a relatively simple design optimization.

The article is organized as follows: Section II derives the scalar potential-based expressions for fringing fields in the geometry shown in Fig. 1. A planar inductor case study is described in Section III, including analytical as well as 2-D finite-element method (FEM) simulation results. Additional effects of H-fields due to winding currents are also addressed in this section. Design optimization is presented in Section IV based on an approximate analytical model supported by comparisons to a more complete analytical model as well as 2-D numerical simulation results. Section V is focused on verification of the analytical design approach using three-dimensional (3-D) FEM simulations. As a practical comparison example, planar inductors are designed using conventional, parallel, and orthogonal air gaps for an 8-kW SiC-based buck converter operating at 250 kHz. Experimental results presented in Section VI confirm more than 45% reduction in ac winding losses compared to the design with standard air gaps. Furthermore, a resonant-circuit test setup is used to experimentally validate quality factor and ac resistance for the prototype inductors with different gap arrangements. Finally, Section VII concludes the article.

II. Analytical Modeling

Fig. 2 shows three planar inductor structures using EI core segments: (a) a conventional structure with standard perpendicular air gaps labeled as p_1, p_2, (b) a structure with parallel (horizontal) air gaps labeled as h_1 [2], [5], and (c) a structure with orthogonal air gaps [19]. In this section, the three cases are compared in terms of the H-field distribution, current distribution, and ac resistance. It is assumed that the planar windings are identical and that the air gaps are selected to obtain approximately the same inductance in all cases. Nonuniform current density and, subsequently, winding losses in the top winding layer depend on the H-field component perpendicular to the conductor [22], [24], denoted as $H_{p1,y}, H_{p2,y}$, and $H_{h1,y}$ in Fig. 2. The underlying assumption is that the copper layers are relatively thin in the y-direction in order to mitigate any possible skin effects at the frequency of interest. Under the assumption that the perpendicular H-field component leads to the dominant fringing-field loss mechanism, which is the case in high-frequency planar inductors, Fig. 2 illustrates the intuition behind advantages and disadvantages of the alternative gap arrangements.

As shown in Fig. 2(c), the effective fringing fields originated from the perpendicular gaps p_1, p_2 and the parallel gap h_1 can be decomposed in the x- and y-directions following the scalar potential-based 1-D method developed in [22]. One may note that $H_{h1,y}$ (y-component of the fringing field produced by gap h_1) acts against the dominant H-field component at both conductor edges, which reduces the effect of current crowding. This field cancelation is in contrast with the case of standard air gaps shown in Fig. 2(a), where the large components of the H-field result in current crowding at the conductor edges.

Moving the gap to the core segment parallel to the windings, as shown in Fig. 2(b), helps mitigate the problem of current crowding at the edges, as discussed in [5]. Compared to Fig. 2(b), without increasing the number of core segments, the orthogonal air-gap approach of Fig. 2(c) offers further improvements in two ways: First, the air gaps are shorter, which reduces magnitude of the fringing fields and, second, the field cancelation further improves uniformity. At the expense of increased complexity, the approach of Fig. 2(b) can be further improved by distributing additional air gaps along the parallel segments of the core [5], [25]. In all cases, however, the orthogonal air-gap approach, which amounts to simple addition of conventionally placed air gaps using a spacer shim between existing core segments, offers further improvements without the need to increase the number of core segments or complexity of the assembly compared to the standard quasidistributed-gap technique described in [5].

Referring to Fig. 1, key geometrical parameters are the gap lengths $2g_1$ and $2g_2$, position Δg, distance y_w from the top surface of the top winding layer to the parallel core segment, distance t_{core} of the windings from the core, winding thickness t_{cu}, spacing t_b between the layers, and winding width $t_w = l - 2t_{\text{core}}$. The core parameters are l, W_c, and W.

The field components of interest at the face of the top winding layer (y_w below the I segment of the core) are [22]

$$H_{g1} = H_{g2} = \frac{0.9NI}{2(2g_1 + g_2)}$$

$$H_{p1,y}(x) = \frac{H_{g1}}{\pi} \tan^{-1}\left(\frac{4xg_1}{x^2 + y_w^2 - 4g_1^2}\right)$$

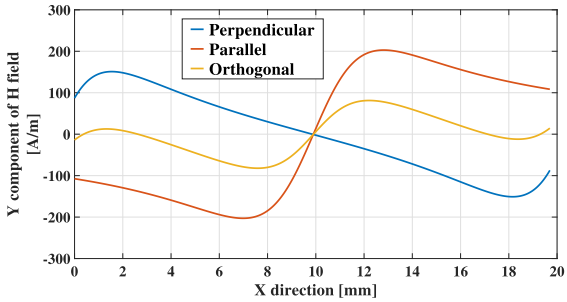

Fig. 3. Distribution of the fringing H-field component perpendicular to the winding at $y_w = 2.8$ mm for the three air-gap arrangements shown in Fig. 2: Perpendicular ($g_1 = 0.435$ mm), parallel ($g_2 = 0.87$ mm), and orthogonal ($g_1 = 0.2175$ mm; $g_2 = 0.435$ mm). In all three cases, inductance is 7 μH.

$$H_{p2,y}(x) = -\frac{H_{g1}}{\pi}\tan^{-1}\left(\frac{4(l-x)g_1}{(l-x)^2 + y_w^2 - 4\,g_1^2}\right)$$
$$H_{h1,y}(x) = \frac{H_{g2}}{2\pi}\ln\left[\frac{y_w^2 + (x - \Delta g + g_2)^2}{y_w^2 + (x - \Delta g - g_2)^2}\right] \quad (1)$$

where

$$t_{\text{core}} \le x \le l - t_{\text{core}} \quad (2)$$

and I is the inductor current. The resultant fringing field, combining the effects of all three gaps, can be found as follows:

$$H_{y,\text{fringing}}(x) = H_{p1,y}(x) - H_{p2,y}(x) - H_{h1,y}(x). \quad (3)$$

From the analytical expressions (1) and (3), the twofold advantages of the orthogonal air gaps can be analyzed. First, to get the same inductance, the additional gaps are shorter, which results in reduced fringing fields, as is the case in all distributed-gap techniques. More importantly, since $H_{h1,y}$ opposes $H_{p1,y}$ and $H_{p2,y}$ at the two conductor edges, respectively, a more uniform distribution of the H-field is obtained, resulting in more uniform current distribution and thereby reduced ac resistance of the top layer. To illustrate this point further, the fringing H-fields in y-direction due to the air gaps in the three different arrangements shown in Fig. 2 are plotted in Fig. 3. The resultant fringing field is most uniform across the face of the top layer conductor in the orthogonal air-gap case of Fig. 2(c), which results in the lowest inductor ac resistance. It should be noted that the number of core segments is the same in Fig. 2(b) and (c).

III. Case Study: High-Frequency Planar Inductor

To illustrate and validate the orthogonal-gap approach of Section II, a case study is used in this section to compare planar inductors with the three different air-gap arrangements shown in Fig. 2. A 7-μH planar inductor is designed using EILP 64 core set including an E-shaped segment ELP 64/10/50 and an I-shaped segment I 64/5/50, with four turns on a four-layer printed circuit board (PCB) having 4-oz copper thickness. The inductor parameters are as follows:

$$N = 4$$
$$t_{\text{cu}} = 0.14\text{ mm},\ t_{\text{core}} = 1\text{ mm},\ t_b = 0.25\text{ mm}$$
$$W = 5.1\text{ mm},\ W_c = 10.2\text{ mm},\ l = 21.7\text{ mm}. \quad (4)$$

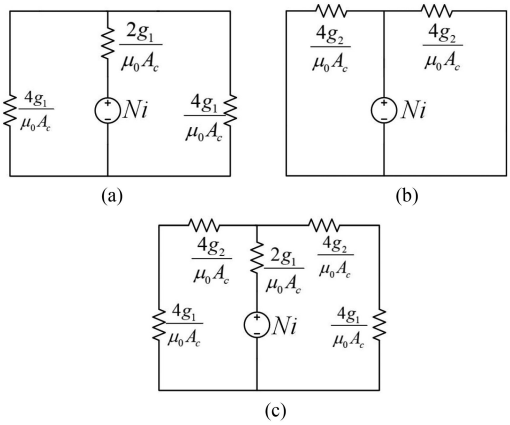

Fig. 4. Equivalent magnetic circuit models for the considered inductors with different air-gap arrangements. (a) Perpendicular. (b) Parallel airgaps. (c) Orthogonal airgaps.

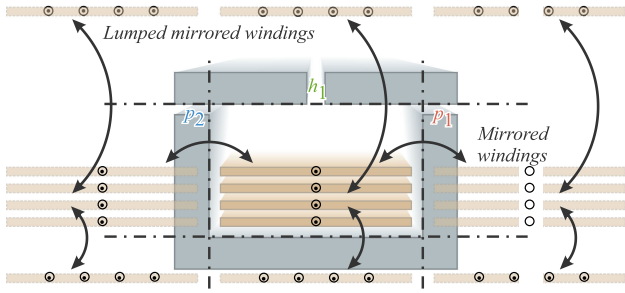

Fig. 5. Mirroring of the windings to account for the H-field effects of the winding currents.

The magnetic circuit models for the three cases considered are shown in Fig. 4, where A_c denotes the geometrical cross-sectional area of the center post of the E core segment, ignoring the fringing flux. In all cases, the gaps are such that the inductance has approximately the same value (7 μH), which uniquely determines the gap lengths g_1 and g_2 in Fig. 4(a) and (b), respectively. In the orthogonal air-gap case, selection of the gap lengths g_1 and g_2, and the position Δg, can be considered a constrained optimization problem, as discussed further in Section IV.

A. H-Fields Due to Winding Currents

The H-field contributions due to fringing are described by (1). To complete the analytical model, it is necessary to consider the H-field effects due to the winding currents. One approach to addressing this issue in an approximate analytical manner is based on mirroring the windings across the core surfaces, as shown in Fig. 5. Currents in the mirrored windings are responsible for creating additional H-fields, which add up to the fringing H-fields. In order to analytically quantify the strength of the H-field, it is assumed that the impact of the winding currents can be taken into account assuming approximately uniform distribution of current I across the winding [11], [22]–[24]. This quasistatic assumption simplifies the analytical model and also makes the model independent of frequency. The assumption is

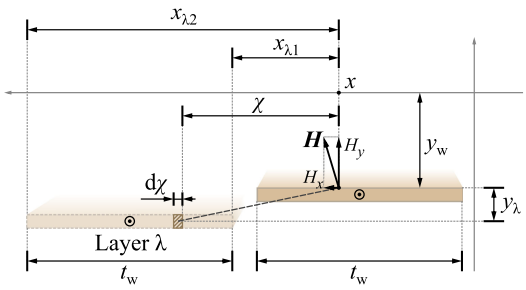

Fig. 6. Calculation of $H_y(x)$ field contributed by winding layer λ on the surface of the top winding layer.

validated by 2-D and 3-D FEM simulations in the subsequent sections.

Under the quasistatic assumption, the y-component of the H-field on the surface of the top winding layer due to winding layer λ can be found from

$$H_{y,\lambda}(x) = \frac{I_\lambda}{2\pi t_w}\int_{x_{\lambda 1}}^{x_{\lambda 2}} \frac{\chi d\chi}{\chi^2 + y_\lambda^2} = \frac{I_\lambda}{4\pi t_w}\ln\frac{x_{\lambda 1}^2 + y_\lambda^2}{x_{\lambda 2}^2 + y_\lambda^2} \tag{5}$$

where the calculation is illustrated in Fig. 6: x_{λ_1} and x_{λ_1} are the x-direction distances of the layer end points with respect to the x-coordinate on the top surface of the top winding layer, y_λ is the vertical distance between layer λ and the top layer, and $t_w = l - 2t_{\text{core}}$ is the layer width.

For each individual winding layer, $I_\lambda = I$. The winding layers mirrored across the I core segment are at least y_w distance away from the points of interest on the top surface of the top layer, whereas the winding layers mirrored across the side and the center post of the E core segment are t_{core} distance away from the top winding layer. In the case considered, which is typical, t_{core} is much smaller than y_w, which justifies the simplifying approach of lumping the corresponding mirrored winding layers into equivalent layers carrying $I_\lambda = 4I$ current, as shown in Fig. 5.

The total field due to the real and the mirrored winding layers can be found as follows:

$$H_{y,\text{windings}}(x) = \sum_{\substack{\lambda=\text{real}\\ \text{and mirrored layers}}} H_{y,\lambda}(x). \tag{6}$$

Finally, the total field in the y-direction, $H_{y,\text{total}}$, can be obtained as the sum of the fringing fields in (3) and the fields due to the winding currents in (6)

$$H_{y,\text{total}}(x) = H_{y,\text{fringing}}(x) + H_{y,\text{windings}}(x). \tag{7}$$

Fig. 7 illustrates a good match between the complete analytical model (7) and 2-D FEM numerical simulation results, validating the assumptions made in the model derivation.

B. Comparison of Inductor Designs Using Different Air-Gap Arrangements

In this section, the inductor designs with air-gap arrangements shown in Fig. 2 are compared in terms of H-field distribution at the face of the top layer conductor. In the conventional design with perpendicular air gaps and in the design with parallel

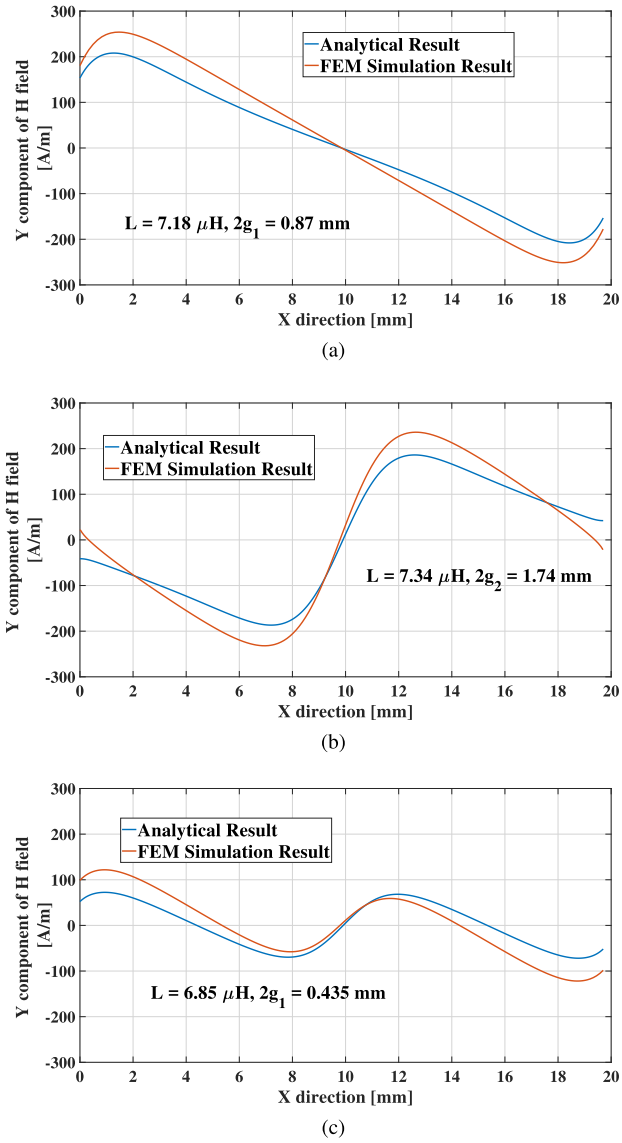

Fig. 7. Comparison of analytical and 2-D FEM simulation results for the distribution of the field $H_{y,\text{total}}$ perpendicular to the windings in the planar inductor at $y_w = 2.8$ mm with (a) conventional air gaps, (b) parallel air gaps, and (c) orthogonal air gaps.

air gaps, the gap lengths are uniquely determined by the inductance specifications. In the orthogonal-gap case, the gap lengths g_1 and g_2 must add up to obtain the same inductance, $2g_1 + g_2 = 2g_{1,\text{conv}}$, where $g_{1,\text{conv}}$ is the gap length in the conventional structure of Fig. 2(a). Subject to this constraint, the optimum gap lengths g_1, g_2 and the placement Δg of gap h_1 can be found to minimize losses. For the case study example, a near-optimum solution based on the analytical optimization framework described in Section IV is

$$\begin{aligned} g_1 &= \frac{g_{1,\text{conv}}}{2} = 0.2175 \text{ mm} \\ g_2 &= g_{1,\text{conv}} = 0.435 \text{ mm} \\ \Delta g &= \frac{l}{2} = 10.9 \text{ mm}. \end{aligned} \tag{8}$$

With all the parameters selected, the total y-component of H-field in (7) at the face of the top layer conductor is plotted in Fig. 7(c) for the optimal orthogonally gapped inductor design. For comparison, $H_{y,\text{total}} = H_{p1,y} - H_{p2,y} + H_{y,\text{windings}}$ and $H_{y,\text{total}} = -H_{h1,y} + H_{y,\text{windings}}$ are also plotted for the conventional (perpendicular) air gaps and for the parallel air-gap cases in Fig. 7(a) and (b), respectively. For a fair comparison, the results in Fig. 7 are obtained using the same value of y_w in all three air-gap arrangements. It can be observed that the H-field distribution is substantially more uniform using the orthogonal gaps compared to the conventional and the parallel air-gap arrangements. One may note that in all three cases in Fig. 7, the y-distance of the top conductor from the parallel core segment (y_w) is relatively small compared to the x-dimension of the core window (l). As a result, fringing-field effects from all air gaps are relatively significant, which is typical for low-profile planar inductors.

It should be noted that the analytical approach does not take into account skin effects and the H-field due to the copper windings in the other window. Nevertheless, the presented model can be considered sufficiently accurate, as illustrated by the good match between the analytical results and the results of 2-D finite-element simulations using Ansys Maxwell, which are overlaid in Fig. 7. In the next section, the analytical model is used to develop simple design guidelines to minimize losses in the orthogonally gapped structure.

IV. Optimization of Orthogonal Air Gaps

The conduction loss per unit length for a thin rectangular conductor is proportional to the square of the y-component of the magnetic field [24]

$$P \propto H_y^2. \tag{9}$$

Under the quasistatic assumption discussed in Section III-A, (9) and therefore the optimization results developed in this section are independent of the excitation frequency. For an orthogonally gapped inductor, focusing on the problem of minimizing losses in the top winding layer, the optimization problem takes the form

$$\begin{aligned} \underset{g_1,g_2,\Delta g}{\text{minimize}} \quad & \int_{t_\text{core}}^{l-t_\text{core}} H_{y,\text{total}}^2(g_1,g_2,\Delta g,x)dx|_{y=-y_w} \\ \text{subject to} \quad & 2g_1 + g_2 = 2g_{1,\text{conv}} \end{aligned} \tag{10}$$

where $2g_{1,\text{conv}}$ is the gap length in the conventional structure of Fig. 2(a). The equidistant gap placement $\Delta g = l/2$ is the best choice, resulting in symmetrical field cancelation on the conductor edges. The problem (10) can be solved numerically in a brute-force manner using an FEM tool, but this approach is computationally inefficient and does not provide design insights. Alternatively, the complete analytical model (7) enables a more efficient numerical solution of the optimization problem (10). To simplify the design and to develop further insights, it is of interest to examine how further simplifications of the analytical model can lead to a near-optimal closed-form solution for the gap lengths.

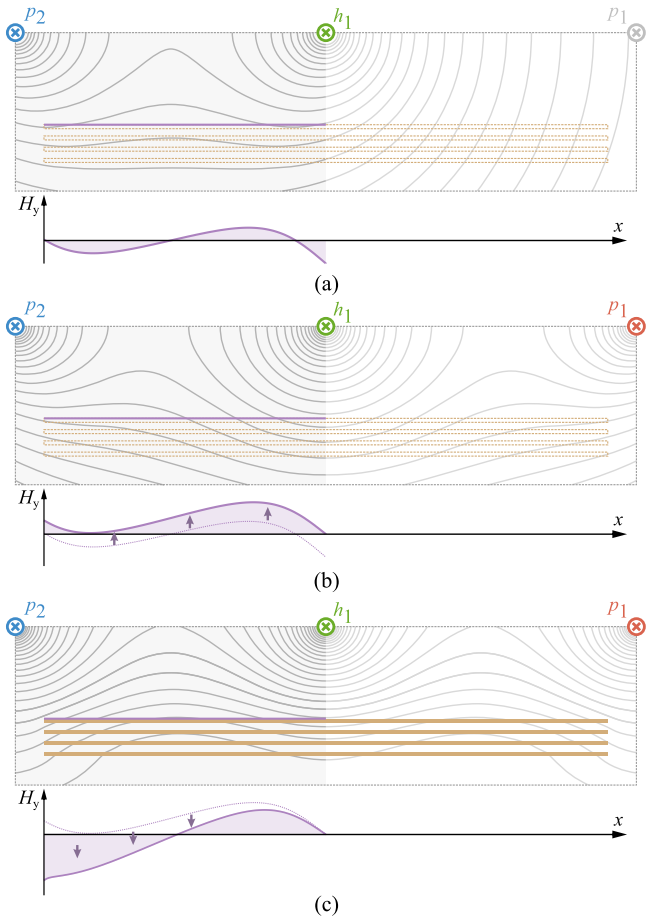

Fig. 8. H-field lines and the resultant H_y field distribution for three cases: (a) according to the simple approximate model (12), which neglects the H-field effects from gap p_1 and from the windings, (b) including the field effects from all gaps, and (c) also including the fields due to the windings. The gap lengths are selected according to (11).

A. Approximate Analytical Solution

In this section, it is shown how the optimization problem (10) allows for a simple, near-optimal closed-form solution

$$g_{1,\text{opt}} = \frac{g_{1,\text{conv}}}{2}, \quad g_{2,\text{opt}} = g_{1,\text{conv}}, \quad \Delta g = \frac{l}{2}. \tag{11}$$

To develop intuition behind the simplifications leading to the closed-form solution (11), Fig. 8 shows contributions to the H-field distribution and their impact on the optimal solution. In all cases shown in Fig. 8, the gap lengths are selected according to (11). Fig. 8(a) illustrates the H-field distribution in the left quarter of the core, according to a model that neglects the H-field effects from gap p_1 and from the windings. It can be observed that H_y is approximately uniform across the x-direction, which is consistent with (11) being an approximate solution to the optimization problem. When the H-field effects originated from p_1 are also taken into account, the H-field distribution shifts slightly upward, as shown in Fig. 8(b), which suggests that the field contribution from h_1 is too strong, and that the gap g_2 should be slightly shorter compared to the value in (11). Finally, Fig. 8(c) shows the complete H-field distribution, which illustrates how the fields originating from the windings counter

the fields due to p_1. As a result, an approximately uniform H-field distribution is in fact obtained using (11).

The solution (11) can be derived based on a simplification of the complete analytical model (3). Motivated by the discussion around Fig. 8, the simplification consists of neglecting the contributions due to winding currents and neglecting the weakest contributions to $H_{y,\text{fringing}}(x)$ following the assumption that fringing fields due to one perpendicular gap do not significantly affect the H-field distribution in a quarter of the core window furthest away from that gap. For example, fringing-field contributions of gap p_1 are neglected for $l/2 \le x \le l - t_{\text{core}}$. As illustrated in Fig. 8, errors due to neglecting contributions due to winding currents and due to further-away gaps partially cancel out.

As detailed in Appendix A, the simplification leads to an approximate piecewise rational expression for $H_y(x)$

$$H_y \approx \begin{cases} 0, & t_{\text{core}} \le x \le y_w \\ \dfrac{H_{g1}}{\pi}\left(\dfrac{4g_1}{x} + \dfrac{4g_2}{2x-l}\right), & y_w \le x \le \frac{l}{2} - y_w \\ 0, & \frac{l}{2} - y_w \le x \le \frac{l}{2} + y_w \\ \dfrac{H_{g1}}{\pi}\left(\dfrac{4g_2}{2x-l} - \dfrac{4g_1}{(l-x)}\right), & \frac{l}{2} + y_w \le x \le l - y_w \\ 0, & l - y_w \le x \le l - t_{\text{core}}. \end{cases} \tag{12}$$

Then, $H_{y,\text{total}} \approx H_y$ enables closed-form evaluation of the integral in (10). Finally, as detailed in Appendix A, the closed-form result for the integral yields the closed-form solution (11) for the orthogonal-gap lengths g_1 and g_2.

In Section III, the solution (11) has been applied to the case study to demonstrate improvements offered by the orthogonal-gap approach in terms of field distribution, current distribution, and ac resistance.

B. Approximation Errors and Sensitivity Analysis

Fig. 9 shows a comparison between numerically computed results for the objective function $\int_{t_{\text{core}}}^{l-t_{\text{core}}} H_y^2 dx$ using the complete analytical model (7) and using the simplified analytical model (12), when air gap g_1 is varied, while meeting the constraint $2g_1 + g_2 = 2g_{1,\text{conv}} = \text{const}$. Although the simplified model and the numerically computed values differ more significantly away from the optimum, the optimum air gap and the minimum of the objective function are well predicted by the simplified model. This is consistent with the arguments provided based on Fig. 8.

It should be noted that the analytical optimization approach neglects the effects of the H-fields produced by the windings themselves. Furthermore, the analysis is simplified by neglecting the weakest fringing-field contributions to the y-component of the fringing field. These simplifying assumptions make the optimization problem analytically tractable but introduce errors. The errors are more significant when the gap arrangements approach the perpendicular or the parallel case. However, as shown in Fig. 9, in the vicinity of the optimum solution, the result based on the simplified analytical model (12) closely matches the result obtained from the complete analytical model (7), which in turn has been validated by 2-D FEM simulation results, as discussed in Section III.

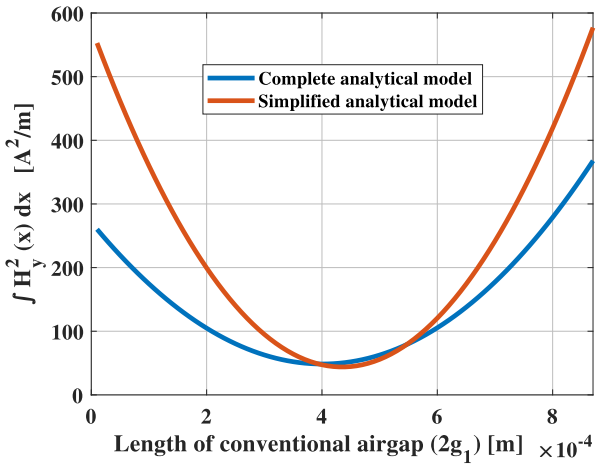

Fig. 9. Cost function in the constraint optimization (10), calculated as a function of gap length $2g_1$ using numerically computed H-field based on the complete analytical model (7) (blue) and using the simplified analytical model (12) (red).

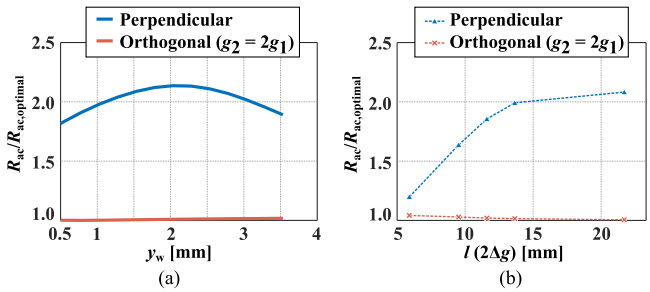

Fig. 10. Sensitivity analysis of the near-optimal solution for the gap lengths (11) with respect to (a) variation in y_w and (b) variation in l.

To investigate validity of the closed-form solution (10) with varying core geometry, Fig. 10 shows results of sensitivity analysis with respect to winding distance y_w and window width l. The value of $R_{\text{ac}}/R_{\text{ac,optimal}}$ is obtained from FEM simulations for the conventionally gapped inductor and for the orthogonally gapped inductor with $g_2 = 2g_1$ according to (11). Fig. 10(a) shows that the simple near-optimal solution (11) results in almost the same R_{ac} as the numerically computed optimal value $R_{\text{ac,optimal}}$ across wide variation of y_w. Similarly, Fig. 10(b) shows that the simple closed-form solution (11) remains close to the numerically obtained optimum over a wide range of core window width l.

V. Design Verification Using 3-D Finite Element Analysis

To further verify the modeling approach presented in Sections II and III and the air-gap optimization approach developed in Section IV, 3-D FEM analyses are carried out based on the inductor 3-D models shown in Fig. 11.

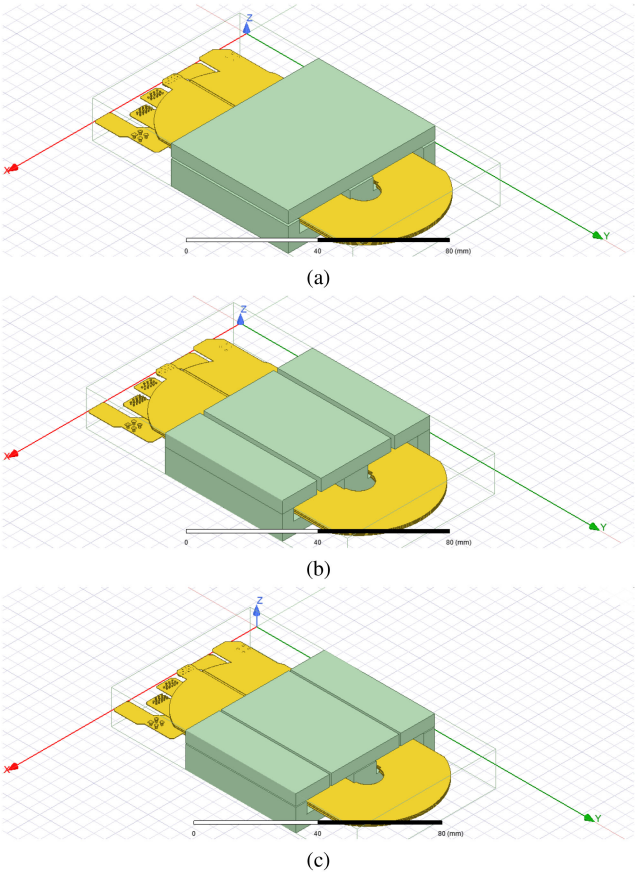

Fig. 11. 3-D FEM model of the planar inductor with (a) conventional air gaps, (b) parallel air gaps, and (c) orthogonal air gaps.

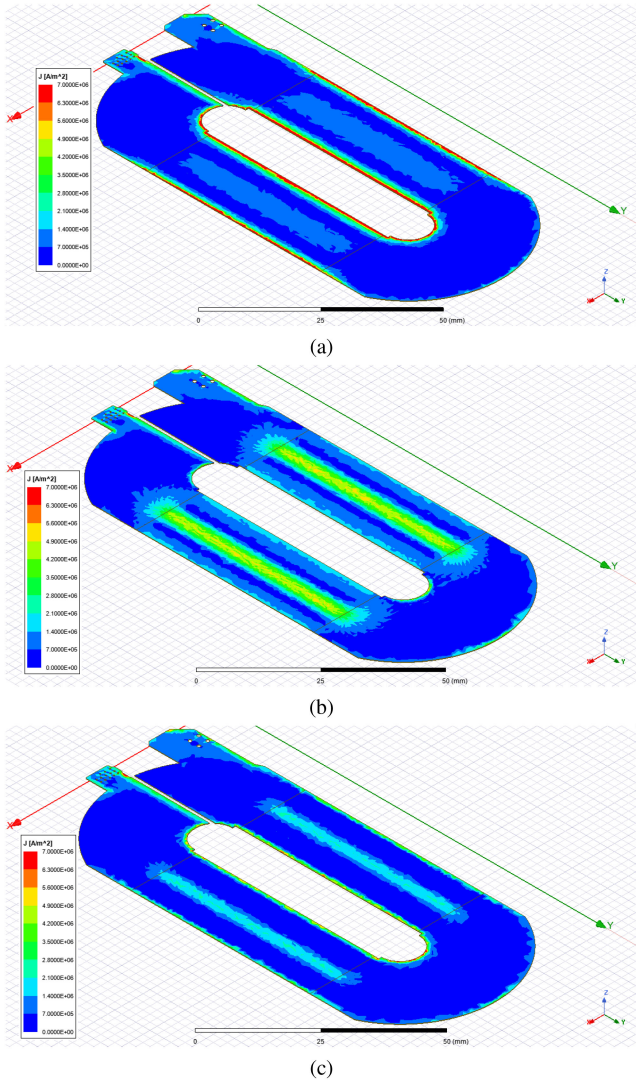

Fig. 12. Current density distribution on the top layer of the planar inductor with (a) conventional air gaps, (b) parallel air gaps, and (c) orthogonal air gaps.

Fig. 12 shows 3-D simulation results for the current density distribution in the top layer of the three cases considered assuming 1-A rms current excitation. For the conventional air-gap arrangement, the numerically calculated inductance is 7.18 μH and the ac resistance of the top winding layer is $R_{\mathrm{ac,top}} = 19\,\mathrm{m\Omega}$ at 250 kHz. Fig. 12(a) illustrates how current crowding at the two conductor edges is the main reason behind increased ac resistance in the conventional structure. The peak current density is $|J|_{\max} = 14.8\,\mathrm{MA/m^2}$ due to 3-D effects near the edges of the windings.

For the parallel air-gap case, the numerically calculated inductance is 7.34 μH, the ac resistance of the top layer is $R_{\mathrm{ac,top}} = 13.5\,\mathrm{m\Omega}$, and the peak current density is reduced to $|J|_{\max} = 5\,\mathrm{MA/m^2}$. Although the current density is reduced, the ac resistance is still larger compared to the orthogonally gapped structure mainly because the parallel gap must be longer to obtain the same inductance. As shown in Fig. 12(b), this larger parallel gap causes the current to crowd over a wider portion in the middle of the winding layer, thus making the effective ac resistance larger.

Fig. 12(c) shows how the current density is much more uniform in the structure with the orthogonally gapped core. The numerically computed inductance remains approximately the same as in the other two cases, 6.85 μH. Some current crowding still occurs at the edges due to 3-D effects, with a maximum current density of $|J|_{\max} = 7\,\mathrm{MA/m^2}$, but the ac resistance of the top layer drops to $R_{\mathrm{ac,top}} = 6.4\,\mathrm{m\Omega}$ at 250 kHz, which corresponds to about 65% reduction in ac winding losses for the top layer compared to the conventionally gapped structure. Compared to the parallel gap case, ac resistance of the top layer is reduced by 53%, while the number of core segments in the structure remains the same. Although the 3-D FEM simulation results show substantial improvement in terms of ac resistance reduction in the top winding layer, it is found that the overall improvements for the four-layer inductor structures are somewhat lower compared to the expectations based on 2-D FEM simulations. This can be explained by looking at the current density distribution in the bottom winding layer as shown in Fig. 13. Fig. 13(a) and (c) shows how perpendicular gaps result in current crowding at the edges of the bottom layers in the conventional and the orthogonally gapped structures. This is simply because of the proximity of the perpendicular gaps to the winding layers and the fact that the field cancelation effects are significant only in the top layer. In contrast, Fig. 13(b) shows uniform current distribution in the bottom layer of the structure

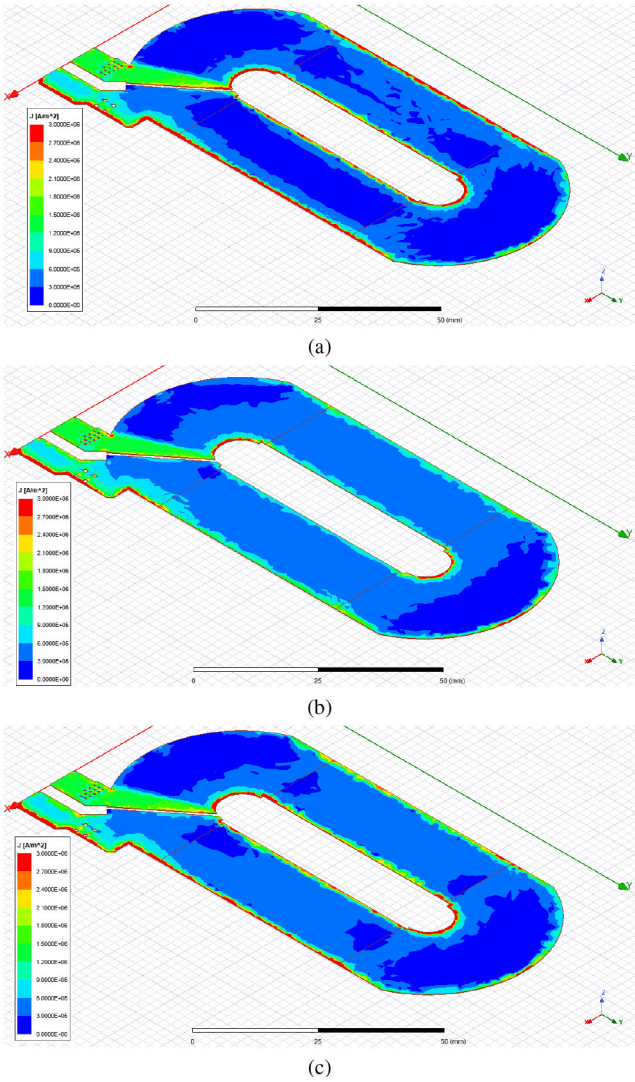

Fig. 13. Current density distribution on the bottom layer of the planar inductor with (a) conventional air gaps, (b) parallel air gaps, and (c) orthogonal air gaps.

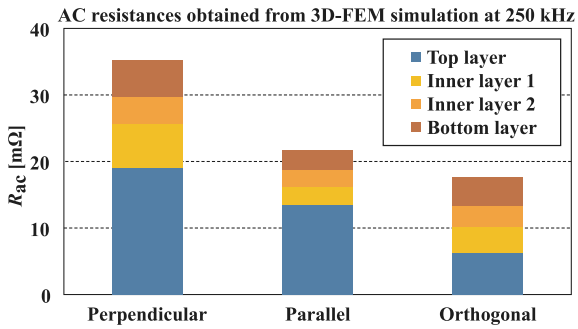

Fig. 14. Distribution of the total ac resistance for the three considered inductors at 250 kHz.

TABLE I
COMPARISON OF MAXIMUM CURRENT DENSITY AND AC RESISTANCE IN THE INDUCTOR WITH 1) CONVENTIONAL AIR GAPS, 2) PARALLEL AIR GAPS, AND 3) ORTHOGONAL AIR GAPS

Air-gap arrangement	f_s [kHz]	$\|J\|_{max}$ [MA/m^2]	$R_{ac,top}$ [mΩ]	$R_{ac,tot}$ [mΩ]
Conventional	100	8.6	13.3	27.7
Fig. 2(a)	250	14.8	19	35.2
Parallel	100	3.5	10.2	18.2
Fig. 2(b)	250	5.0	13.5	21.7
Orthogonal	100	4.0	4.8	14.6
Fig. 2(c)	250	7.0	6.4	17.6

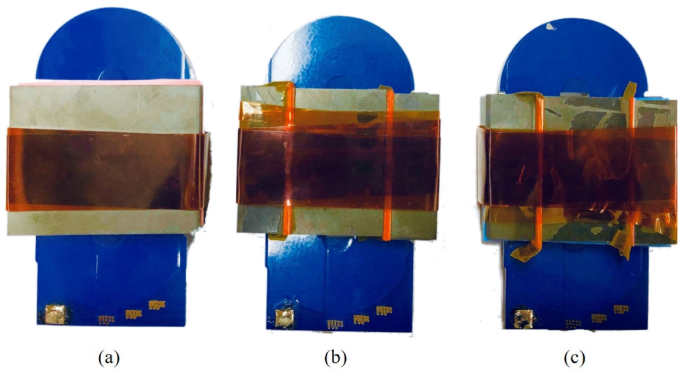

Fig. 15. Planar inductor prototypes using EILP 64 core set with (a) conventional air gaps, (b) parallel air gaps, and (c) orthogonal air gaps.

with parallel gaps with much less current crowding at the edges due to only the proximity H-fields generated by the windings. Because of these 3-D effects, the overall improvement offered by the orthogonally gapped inductor is reduced compared to the expectations based on the analytical model and the 2-D analysis, which are focused on the effects in the top layer only. Numerically computed ac resistances at 250 kHz for the bottom layer of the conventional, parallel, and orthogonal structures are, respectively, 5.4, 3, and 4.2 mΩ.

Fig. 14 shows how the ac resistance obtained by 3-D FEM simulation is distributed among the four layers of the windings for the three considered inductors with 250-kHz excitation. In all three cases, the majority of the loss occurs in the top layer, which justifies the simplified model and the optimization approach developed in Sections II–IV. However, the loss in the bottom layer is larger in the conventional and the orthogonally gapped structures compared to the structure with parallel air gaps. Table I summarizes 3-D finite-element simulation results for the three considered air-gap arrangements in terms of the maximum current density, the ac resistance of the top winding layer, and the overall ac resistance at two different frequencies: 100 and 250 kHz. The orthogonally gapped inductor has the overall ac resistance reduced by approximately 50% compared to the conventionally gapped inductor and by approximately 19% compared to the structure with parallel air gaps.

VI. EXPERIMENTAL VALIDATION

Experimental inductor prototypes based on the case-study designs discussed in Sections II–V are shown in Fig. 15. All inductors have the same core size, the same PCB windings and approximately the same inductance but differ in the air-gap arrangement: Conventional air gaps in Fig. 15(a), parallel air gaps in Fig. 15(b), and orthogonal air gaps in Fig. 15(c). The inductor parameters are summarized in Section III, with the gap

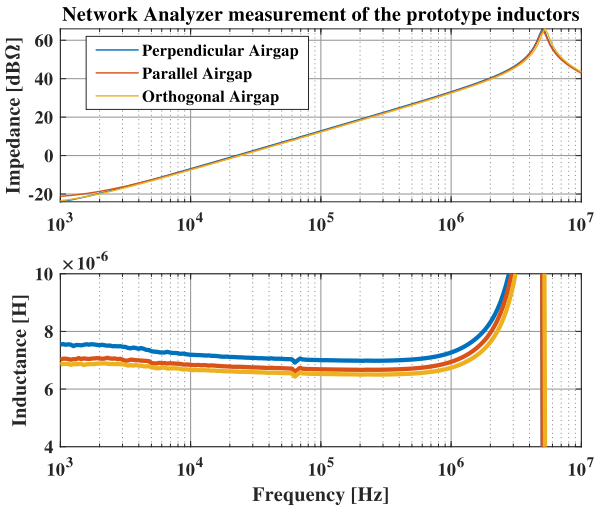

Fig. 16. Network analyzer measurements using Omicron Lab's Bode 100 instrument of perpendicular (blue), parallel (red), and orthogonal (yellow) structures demonstrating the impedance and the inductance measured by the instrument over a wide frequency range.

lengths provided in (8). The core material for all three prototypes is TDK N87.

Controlled thickness (0.0127 mm) shims were used to implement the air gaps so that all three prototypes have the desired inductance of approximately 7 μH. Fig. 16 shows the impedance magnitude plots and the inductances measured over a range of frequencies using a Bode 100 network analyzer. In all three cases, the inductance remains approximately the same over a wide range of frequencies. The self-resonant frequency in all three prototypes is around 5 MHz, well above the intended operating frequency, and all three inductors have essentially the same peak impedance of approximately 2 kΩ.

The way the prototypes and the air gaps are constructed affects the location of the origin, which is tied to the I core segment, as shown in Fig. 1. As a result, given that the winding location and the E core segment are fixed, the distance y_w from the origin to the top winding depends on the gap length g_1 and differs slightly in the three air-gap arrangements considered: $y_w = 3.67$ mm (conventional), $y_w = 2.8$ mm (parallel), and $y_w = 3.23$ mm (orthogonal). 3-D FEM simulation results show that the 16% larger y_w (3.23 mm compared to 2.8 mm) accounts for approximately 5% decrease in ac resistance at 100 kHz and approximately 6% decrease in ac resistance at 250 kHz in the prototype with orthogonal air gaps.

Experimental validation results include a comparison of losses in a converter prototype shown in Fig. 17(a) and measurements of the inductor Q factor and ac resistance in a resonant circuit shown in Fig. 17(b).

A. Comparison of Losses in a Converter Prototype

The prototype inductors are used in an SiC-based 8-kW synchronous Buck converter operating at 250 kHz at 50% duty ratio. To verify the predicted loss reduction, the converter is operated unloaded, and the losses are determined by measuring the input dc power as shown in Fig. 17(a), using Agilent 5-1/2

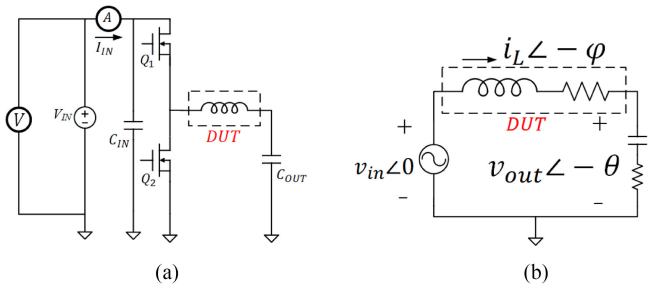

Fig. 17. Diagrams of the circuits used in experimental verification. (a) Unloaded zero voltage switching (ZVS) buck converter. (b) Resonant circuit.

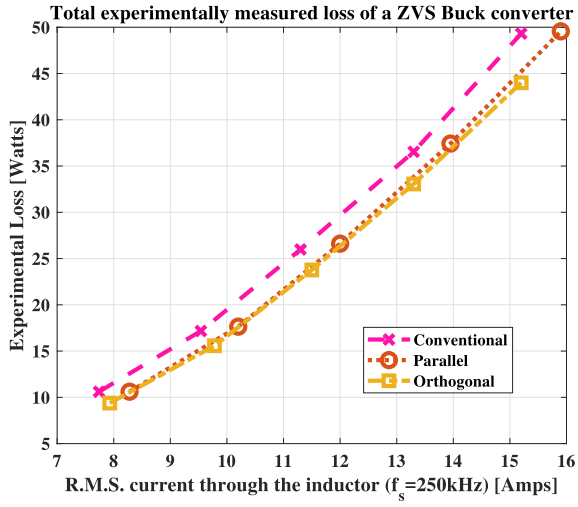

Fig. 18. Comparisons of total measured converter losses in the prototypes with conventional air gaps (purple), parallel air gaps (red), and orthogonal air gaps (yellow).

digit precision multimeters, with input voltage varying from 200 to 400 V. The inductor current has a triangular shape with zero dc bias and a peak value proportional to the input voltage. The converter operates with zero voltage switching of both transistors so that switching losses are relatively low.

The total converter loss as a function of the inductor rms current is compared in Fig. 18 for the conventionally gapped inductor, the parallel gapped inductor, and for the orthogonally gapped inductor. Other than the inductor, all other converter components remain the same. Since the inductances are also approximately the same, operating at the same input voltage results in approximately the same current waveforms and the same rms current. Therefore, the switch conduction and switching losses, core losses, as well as losses associated with PCB traces remain approximately the same when the converter is operated at the same input voltage. In conclusion, since all other losses are approximately the same under the same operating conditions, the experimentally measured loss difference can be used to estimate the reduction in ac winding losses.

Fig. 19 shows the difference in loss between the inductors with orthogonal and perpendicular air gaps (top) and between the inductors with orthogonal and parallel air gaps (bottom) as functions of the rms current. The loss-difference curves shown include data points based on measurements and based on 3-D

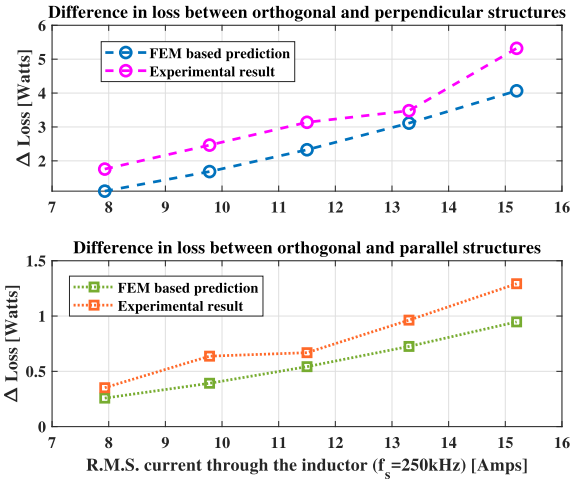

Fig. 19. Experimentally measured and theoretically predicted loss difference in the converter prototype of Fig. 17(a) between the orthogonal structure and the perpendicular structure (top) and between the orthogonal structure and the parallel structure (bottom).

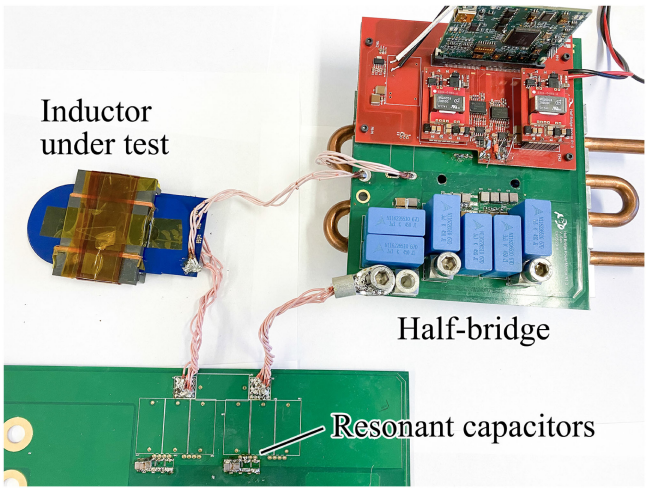

Fig. 20. Experimental test setup using a half bridge circuit to excite the resonant tank in Fig. 17(b).

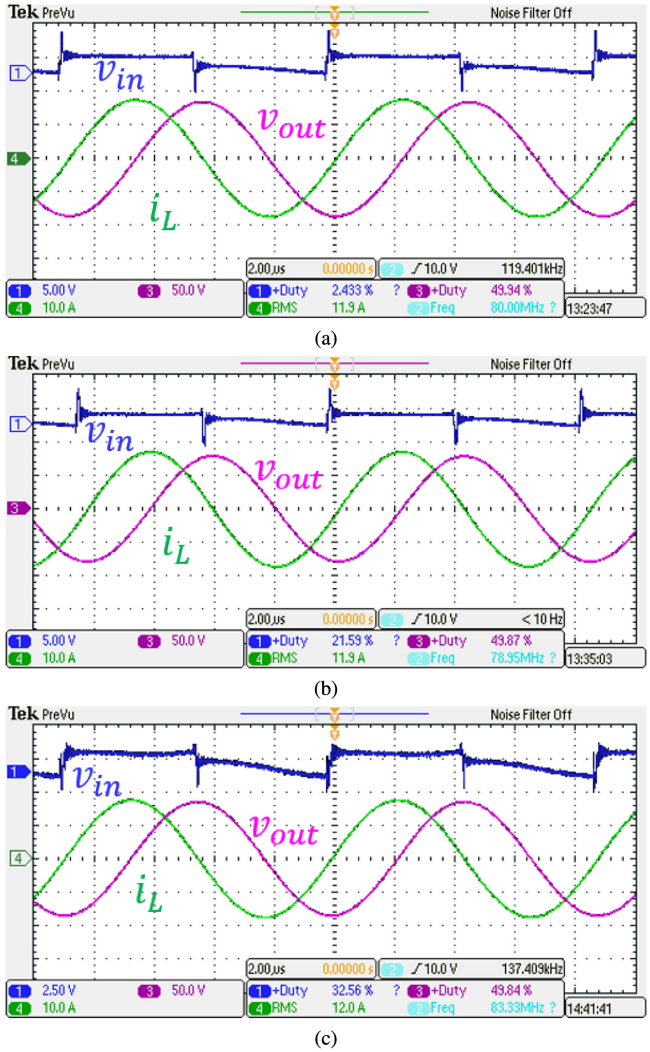

Fig. 21. Experimental resonant circuit waveforms for (a) perpendicular, (b) parallel, and (c) orthogonal structures under test. The rms current in all three experiments are kept constant at 12 A. The excitation frequencies and the measured losses are summarized in Table II.

FEM simulation results listed in Table I. A relatively close match between 3-D FEM and experimental results can be observed, validating approximately 50% loss reduction offered by the orthogonally gapped inductor compared to the conventionally gapped inductor and approximately 19% loss reduction compared to the inductor with parallel air gaps.

B. Quality Factor and AC Resistance

To provide further experimental verification, the inductor quality factor has been measured using a resonant-circuit based setup described in [26]. A slightly modified version of this setup is used to measure the total loss in the inductor at a certain frequency of operation. The circuit schematic is shown in Fig. 17(b) and the experimental setup using a half bridge to generate the excitation v_{in} is shown in Fig. 20. A resonant circuit is formed to reduce the effect of reactive power and thus improve accuracy. Assuming perfect resonance, the quality factor is given by $Q = v_{\text{out}}/v_{\text{in}}$. Since achieving perfect resonance is cumbersome in practice, another approach is to find the active power in the circuit

$$P_{\text{loss}} = \frac{v_{\text{in}} i_L}{2} \cos(\phi). \tag{13}$$

Assuming that the resonant capacitor has very low equivalent series resistance (ESR), the entire loss is on the inductor and is indicative of its quality factor. In the experimental setup, six COG/NP0 47-nF capacitors (TDK C4532C0G) are connected in parallel to realize the resonant capacitor and to meet the low-ESR assumption. The resonant frequency for the 7-μH inductance is

$$f_{\text{res}} = \frac{1}{2\pi\sqrt{\text{LC}}} = 113 \text{ kHz}. \tag{14}$$

Since the current through the inductor is purely sinusoidal without any dc bias, core losses can be estimated using Steinmetz expression [27], [28]. The ac resistance of the inductor can then

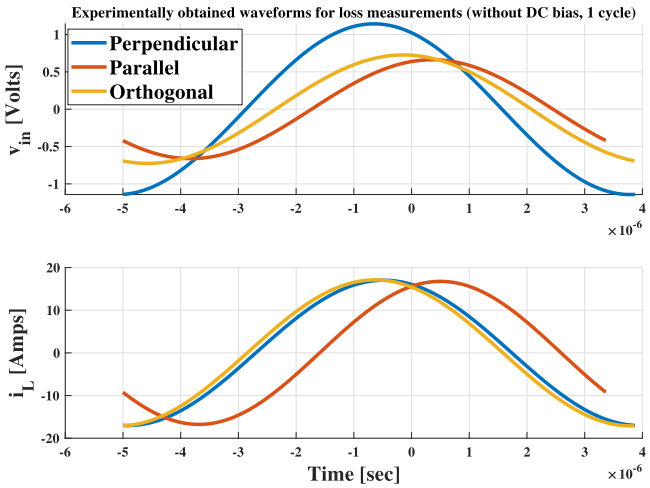

Fig. 22. Experimentally obtained voltage and current waveforms in the resonant circuit prototype with the inductors using conventional air gaps (blue), parallel air gaps (red), and orthogonal air gaps (yellow).

TABLE II
EXPERIMENTALLY MEASURED AC RESISTANCE OF THE INDUCTOR WITH 1) CONVENTIONAL AIR GAPS, 2) PARALLEL AIR GAPS, AND 3) ORTHOGONAL AIR GAPS

Air-gap arrangement	f_s	Winding loss	R_{ac}
Conventional	112.7 kHz	6.4 W [12.0 A rms]	38 mΩ
Parallel	119.5 kHz	4.6 W [11.9 A rms]	30 mΩ
Orthogonal	112.8 kHz	4.2 W [12.1 A rms]	25 mΩ

be identified from the winding loss

$$R_{\text{ac}} = \frac{P_{\text{loss}} - K_{fe}(\Delta B)^{\beta} f^{\alpha} V_e}{I_L^2};\ \Delta B = \frac{L i_L}{nA} \tag{15}$$

where K_{fe}, α, and β are the Steinmetz parameters for the core material, n is the number of turns, V_e is the effective core volume, and A is the core cross-sectional area. Current i_L is the peak of the inductor current and I_L is the inductor rms current. Additionally, as discussed in Appendix B, experiments were performed to verify that placing orthogonal gaps by modifying the I core segment does not effect the core losses. Fig. 26 shows that the cores with or without air gaps in the I segment have almost the same core loss density. Hence, (15) can be used to estimate the ac winding resistances.

Experimentally obtained voltage and current waveforms for the three cases considered are shown in Fig. 21. Since a half bridge is used to excite the resonant tank, the switch node voltage v_{in} contains harmonics. The fundamental component of v_{in} is shown in Fig. 22 along with the resonant current for the three cases considered. Delay associated with the current measurement using a high bandwidth current probe has been calibrated and compensated during loss calculation using a 10-mΩ, 3-W, ±0.1% precision resistor from Vishay.

Based on the experimental results, the estimated values of R_{ac} are summarized in Table II. A comparison with the numerically computed ac resistances summarized in Table I shows that the experimentally obtained ac resistances follow the same trend, while the values differ by an offset of approximately 10 mΩ in all three cases. This offset can be attributed to parasitic series resistances in the resonant circuit.

VII. CONCLUSION

A simple orthogonal-gap technique is proposed to reduce effects of fringing fields in high-frequency inductors. The approach can be applied to various magnetic structures and amounts to distributing air gaps between core segments perpendicular to the windings and segments parallel with the windings. In a planar inductor, the perpendicular air gaps are added conventionally, simply by inserting a spacer between planar core segments, without the need to increase the number of core segments or complexity of the assembly. A 1-D analytical approach [22] is applied to derive H-field distribution and to optimize the gap lengths to reduce inductor ac losses. An analytical optimization framework is developed, which yields simple design guidelines verified by 2-D and 3-D FEM simulations. As a case study, a planar inductor is designed for an 8-kW SiC-based buck converter operating at 250 kHz. 3-D FEM simulations along with experimental results are provided to compare the air-gap arrangements and to verify approximately 50% reduction in ac winding losses using the orthogonal air gaps compared to a conventional design. Compared to structures with parallel air gaps, overall improvements are reduced due to 3-D effects resulting in current crowding at the edges of inner and bottom layers of an orthogonally gapped inductor. Nevertheless, 3-D FEM analysis and experimental results show that the optimized orthogonally gapped inductor has approximately 19% smaller ac resistance compared to an inductor having parallel air gaps and the same number of core segments.

APPENDIX A
APPROXIMATE ANALYTICAL MODEL

The y-component of the fringing field due to gap p_1 in (1) can be approximated as follows:

$$H_{p1,y}(x) = \frac{H_{g1}}{\pi} \tan^{-1}\left(\frac{4xg_1}{x^2 + y_w^2 - 4g_1^2}\right) \approx \frac{H_{g1}}{\pi} \frac{4xg_1}{x^2 + y_w^2 - 4\,g_1^2}. \tag{16}$$

This expression can be further approximated as follows:

$$H_{p1,y}(x) \approx \begin{cases} 0, & t_{\text{core}} \le x \le y_w \\ \dfrac{H_{g1}}{\pi}\left(\dfrac{4g_1}{x}\right), & y_w \le x \le \frac{l}{2} - y_w \\ 0, & \frac{l}{2} - y_w \le x \le l - t_{\text{core}}. \end{cases} \tag{17}$$

The approximation is justified by the fact that the strength of this field is much weaker compared to the fields due to p_2 and h_1 in the left quarter of the core window ($l/2 - y_w \le x \le l - t_{\text{core}}$) and in low profile planar magnetic structures where the distance y_w is relatively short.

Similarly, the y-component of the H-field due to gap p_2 can be approximated as follows:

$$H_{p2,y}(x) = -\frac{H_{g1}}{\pi}\tan^{-1}\frac{4(l-x)g_1}{(l-x)^2+y_w^2-4g_1^2} \approx -\frac{H_{g1}}{\pi}\frac{4(l-x)g_1}{(l-x)^2+y_w^2-4g_1^2} \tag{18}$$

and

$$H_{p2,y}(x) \approx \begin{cases} 0, & t_{\text{core}} \le x \le \frac{l}{2}+y_w \\ -\frac{H_{g1}}{\pi}\left(\frac{4g_1}{l-x}\right), & \frac{l}{2}+y_w \le x \le l-y_w \\ 0, & l-y_w \le x \le l-t_{\text{core}}. \end{cases} \tag{19}$$

Finally, assuming $\Delta g = l/2$, the y-component of the H-field due to the horizontal gap h_1 can be approximated as follows:

$$H_{h1,y}(x) = \frac{H_{g2}}{2\pi}\ln\left[\frac{y_w^2+(x-\Delta g+g_2)^2}{y_w^2+(x-\Delta g-g_2)^2}\right] = \frac{H_{g2}}{2\pi}\ln\left[1+\frac{4(x-\Delta g)g_2}{y_w^2+(x-\Delta g-g_2)^2}\right] \approx \frac{H_{g2}}{2\pi}\frac{4(x-\frac{l}{2})g_2}{y_w^2+(x-\frac{l}{2}-g_2)^2} \tag{20}$$

which can be further approximated to

$$H_{h1,y}(x) \approx \begin{cases} 0, & \frac{l}{2}-y_w \le x \le \frac{l}{2}+y_w \\ \frac{H_{g2}}{\pi}\left(\frac{4g_2}{2x-l}\right), & t_{\text{core}} \le x \le \frac{l}{2}-y_w \\ \frac{H_{g2}}{\pi}\left(\frac{4g_2}{2x-l}\right), & \frac{l}{2}+y_w \le x \le l-t_{\text{core}}. \end{cases} \tag{21}$$

Since $H_{g1} = H_{g2}$, by combining (17), (19), and (21), the total y-component H_y of the field due to the air gaps can be expressed as follows:

$$H_y(x) \approx \begin{cases} 0, & t_{\text{core}} \le x \le y_w \\ \frac{H_{g1}}{\pi}\left(\frac{4g_1}{x}+\frac{4g_2}{2x-l}\right), & y_w \le x \le \frac{l}{2}-y_w \\ 0, & \frac{l}{2}-y_w \le x \le \frac{l}{2}+y_w \\ \frac{H_{g1}}{\pi}\left(\frac{4g_2}{2x-l}-\frac{4g_1}{(l-x)}\right), & \frac{l}{2}+y_w \le x \le l-y_w \\ 0, & l-y_w \le x \le l-t_{\text{core}}. \end{cases} \tag{22}$$

This is a piecewise rational function approximately representing (3). The objective is to

$$\underset{g_1,g_2,\Delta g}{\text{minimize}} \quad \int_{t_{\text{core}}}^{l-t_{\text{core}}} H_y^2(g_1,g_2,\Delta g,x)dx|_{y=-y_w} \qquad \text{subject to} \quad 2g_1+g_2 = 2g_{1,\text{conv}}. \tag{23}$$

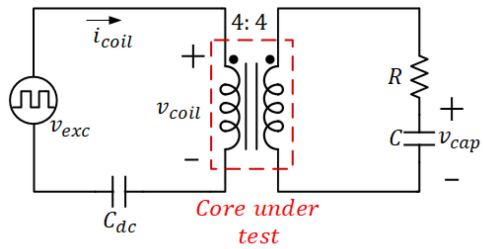

Fig. 23. Schematic of the circuit used to measure core loss using the standard EI core and the customized ore with gaps in the I core segment.

Since $\Delta g = l/2$, $g_2 = 2g_{1,\text{conv}} - 2g_1$, the cost function can be found as

$$H^2 = \int_{t_{\text{core}}}^{l-t_{\text{core}}} H_y^2 dx \approx \int_{y_w}^{\frac{l}{2}-y_w} \frac{H_{g1}^2}{\pi^2}\left(\frac{4g_1}{x}+\frac{8(g_{1,\text{conv}}-g_1)}{2x-l}\right)^2 dx + \int_{\frac{l}{2}+y_w}^{l-y_w} \frac{H_{g1}^2}{\pi^2}\left(\frac{8(g_{1,\text{conv}}-g_1)}{2x-l}-\frac{4g_1}{(l-x)}\right)^2 dx \tag{24}$$

which yields

$$H^2 = \frac{H_{g1}^2}{\pi^2}\left[\left[32\,g_1^2+32(g_{1,\text{conv}}-g_1)^2\right]\left[\frac{1}{y_w}-\frac{2}{l-2y_w}\right] - 256\,\frac{g_1(g_{1,\text{conv}}-g_1)}{l}\ln\left(\frac{l-2y_w}{2y_w}\right)\right]. \tag{25}$$

To minimize H^2, solving

$$\frac{\partial H^2}{\partial g_1} = 0 \tag{26}$$

results in the solution (11) for the gap lengths

$$g_1 = \frac{g_{1,\text{conv}}}{2}, g_2 = g_{1,\text{conv}}, \Delta g = l/2. \tag{27}$$

APPENDIX B
CORE LOSS MEASUREMENT

To verify that the core loss remains approximately the same with the customization of the I core segment, a test setup to measure core loss was constructed using the approach presented in [29]. The circuit schematic is shown in Fig. 23 and the relevant hardware using a half bridge excitation and an RC integrator is shown in Fig. 24. In Fig. 23, the auxiliary coil enables integration of the volt-seconds applied to the core. Capacitor voltage v_{cap} is a proxy for the flux density (B) in the core, whereas the primary side current i_{coil} serves as a way to measure the magnetic H-field

$$H(t) = \frac{Ni_{\text{coil}}(t)}{\mu_r l_g + l_c}; B(t) = \frac{\int v_{\text{coil}}(t)dt}{NA} = \frac{v_{\text{cap}}(t)\text{RC}}{NA} \tag{28}$$

where l_c denotes the mean length of the magnetic flux path determined from the core geometry, l_g is the air-gap length, μ_r is the relative permeability of the core material, N denotes the number of primary and secondary turns, and A is the cross-sectional area of the core. In order to avoid any H-field cancelation, the

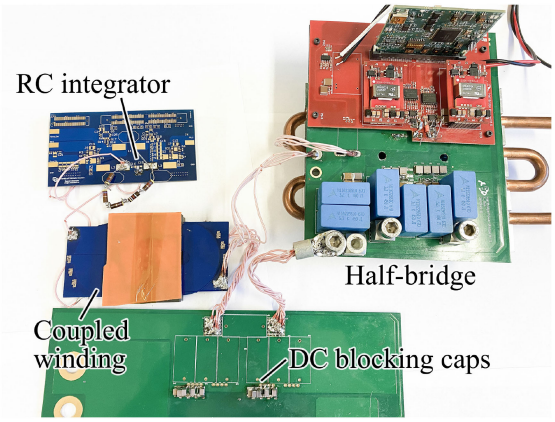

Fig. 24. Test setup using a half bridge circuit, an additional coupled coil loaded by an RC integrator with the inductor implementing the circuit of Fig. 23.

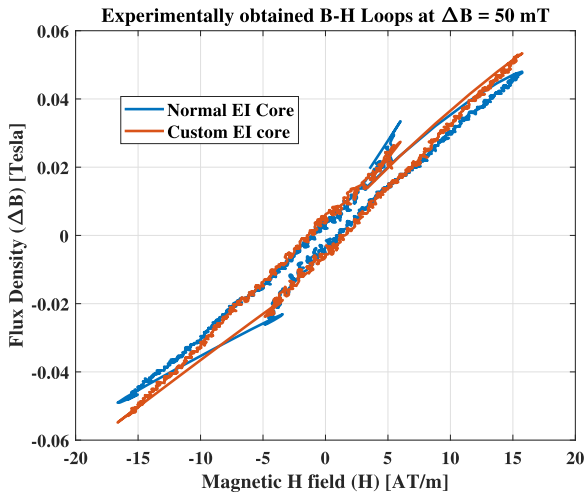

Fig. 25. Experimentally obtained B-H loops for the standard and the custom EI cores at $\Delta B = 50$ mT.

secondary current should be very small compared to the primary current in Fig. 23. This can be achieved using a relatively high value of R. Another design criterion of the integrator is that the RC time constant should be much higher than the time period of the square wave excitation so that the capacitor acts as an integrator. Both the standard and the customized EI cores were tested using the test setup of Fig. 24. In the experiment, the switching frequency was 113 kHz. $R = 23.85\ \text{k}\Omega$ along with $C = 10$ nF. Very small air gaps were inserted between the core segments to facilitate easier estimation of H-field from the sensed current. Similar to the Q factor measurement test setup, switching of the half bridge creates additional noise in the experimentally obtained waveforms. To filter the noise, the oscilloscope measured voltage and current data sampled at 1 ns were postprocessed by discarding outliers around switching transitions and by low-pass filtering with 10-MHz bandwidth. The resulting B-H loops are illustrated in Fig. 25 for the standard EI core and for the custom EI core with additional gaps. Similar experiments were performed for different levels of ΔB and the filtered data was used to calculate the core loss density in both

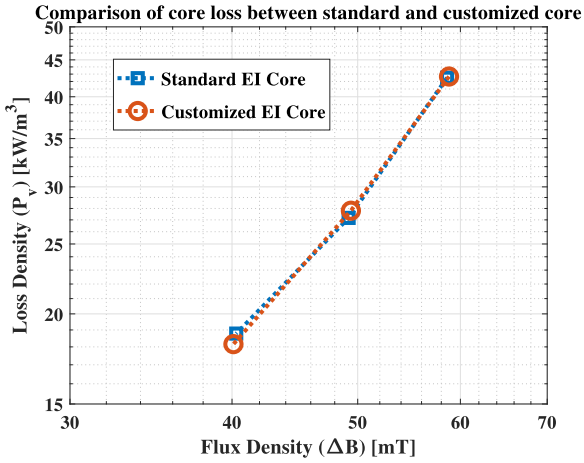

Fig. 26. Comparison of experimentally obtained core loss density for the standard and the customized EI cores.

core types using

$$P_v = \int H dB \tag{29}$$

The core material (TDK N87) is a MnZn ferrite suitable for high-frequency applications. As a result, eddy current losses are relatively small and can be neglected in the core loss comparison. Finally, Fig. 26 shows a comparison of the measured core losses for the standard and the customized core as functions of ΔB. The experimental results conclusively show that both cores have very similar core loss density, which in turn implies that machining the I core segment did not introduce additional losses in the experimental inductor prototype.

ACKNOWLEDGMENT

The views and opinions of authors expressed herein do not necessarily state or reflect those of the United States Government or any agency thereof.

REFERENCES

[1] W. M. Chew, P. D. Evans, and W. J. Heffernan, "High frequency inductor design concepts," in *Proc. PESC'91 Rec. 22nd Annu. IEEE Power Electron. Specialists Conf.*, Jun. 1991, pp. 673–678.

[2] Z. Ouyang and M. A. E. Andersen, "Overview of planar magnetic technology fundamental properties," *IEEE Trans. Power Electron.*, vol. 29, no. 9, pp. 4888–4900, Sep. 2014.

[3] C. R. Sullivan, "Prospects for advances in power magnetics," in *Proc. 9th Int. Conf. Integr. Power Electron. Syst.*, Mar. 2016, pp. 1–9.

[4] B. A. Reese and C. R. Sullivan, "Litz wire in the MHz range: Modeling and improved designs," in *Proc. IEEE 18th Workshop Control Model. Power Electron.*, Jul. 2017, pp. 1–8.

[5] J. Hu and C. R. Sullivan, "Ac resistance of planar power inductors and the quasidistributed gap technique," *IEEE Trans. Power Electron.*, vol. 16, no. 4, pp. 558–567, Jul. 2001.

[6] K. D. T. Ngo and M. H. Kuo, "Effects of air gaps on winding loss in high-frequency planar magnetics," in *Proc. PESC'88 Rec., 19th Annu. IEEE Power Electron. Specialists Conf.*, vol. 2, Apr. 1988, pp. 1112–1119.

[7] R. A. Jensen and C. R. Sullivan, "Optimal core dimensional ratios for minimizing winding loss in high-frequency gapped-inductor windings," in *Proc. 18th Annu. IEEE Appl. Power Electron. Conf. Expo.*, vol. 2, Feb. 2003, pp. 1164–1169.

[8] L. Daniel, C. R. Sullivan, and S. R. Sanders, "Design of microfabricated inductors," *IEEE Trans. Power Electron.*, vol. 14, no. 4, pp. 709–723, Jul. 1999.

[9] L. Wang, Z. Hu, Y. Liu, Y. Pei, and X. Yang, "Multipermeability inductors for increasing the inductance and improving the efficiency of high-frequency DC/DC converters," *IEEE Trans. Power Electron.*, vol. 28, no. 9, pp. 4402–4413, Sep. 2013.
[10] T. Ge, K. D. T. Ngo, and J. Moss, "Two-dimensional gapping to reduce light-load loss of point-of-load inductor," *IEEE Trans. Power Electron.*, vol. 32, no. 1, pp. 540–550, Jan. 2017.
[11] J. Schafer, D. Bortis, and J. W. Kolar, "Optimal design of highly efficient and highly compact PCB winding inductors," in *Proc. IEEE 19th Workshop Control Model. Power Electron.*, Jun. 2018, pp. 1–8.
[12] J. Knowles, "The origin of the increase in magnetic loss induced by machining ferrites," *IEEE Trans. Magn.*, vol. 11, no. 1, pp. 44–50, Jan. 1975.
[13] S. Chandrasekar, M. C. Shaw, and B. Bhushan, "Comparison of grinding and lapping of ferrites and metals," *J. Trinology*, vol. 109, no. 2, pp. 76–82, May 1987.
[14] Y. Wang, G. Calderon-Lopez, and A. J. Forsyth, "High-frequency gap losses in nanocrystalline cores," *IEEE Trans. Power Electron.*, vol. 32, no. 6, pp. 4683–4690, Jun. 2017.
[15] E. Stern and D. Temme, "Magnetostriation effects in remanence phase shifters (correspondence)," *IEEE Trans. Microw. Theory Tech.*, vol. 13, no. 6, pp. 873–874, Nov. 1965.
[16] J. Hu and C. R. Sullivan, "Analytical method for generalization of numerically optimized inductor winding shapes," in *Proc. 30th Annu. IEEE Power Electron. Specialists Conf. Rec. (Cat. No.99CH36321)*, vol. 1, Jul. 1999, pp. 568–573.
[17] J. D. Pollock and C. R. Sullivan, "Loss models for shaped foil windings on low-permeability cores," in *Proc. IEEE Power Electron. Specialists Conf.*, Jun. 2008, pp. 3122–3128.
[18] N. Simpson and P. H. Mellor, "Additive manufacturing of shaped profile windings for minimal AC loss in electrical machines," in *Proc. IEEE Energy Convers. Congr. Exp.*, Sep. 2018, pp. 5765–5772.
[19] S. Mukherjee *et al.*, "AC resistance reduction using orthogonal air gaps in high frequency inductors," in *Proc. 20th Workshop Control Model. Power Electron.*, Jun. 2019, pp. 1–6.
[20] W. K. Mo, K. M. Paasch, and M. Sachmann, "Optimal inductor winding geometries for minimizing winding loss in gapped inductor designs," in *Proc. 19th Eur. Conf. Power Electron. Appl.*, Sep. 2017, pp. P.1–P.6.
[21] A. F. Goldberg, "Development of magnetic components for 1–10 MHz dc-dc converters," Ph.D. dissertation, MIT, Cambridge, MA, USA, Sep. 1988.
[22] W. A. Roshen, "Fringing field formulas and winding loss due to an air gap," *IEEE Trans. Magn.*, vol. 43, no. 8, pp. 3387–3394, Aug. 2007.
[23] W. A. Roshen, "High-frequency fringing fields loss in thick rectangular and round wire windings," *IEEE Trans. Magn.*, vol. 44, no. 10, pp. 2396–2401, Oct. 2008.
[24] E. Snelling, *Soft Ferrites: Properties and Applications*. London, U.K.: Butterworth, 1988.
[25] J. Hu and C. R. Sullivan, "Optimization of shapes for round-wire high-frequency gapped-inductor windings," in *Proc. Conf. Rec. IEEE Ind. Appl. Conf. 33rd IAS Annu. Meeting (Cat. No.98CH36242)*, vol. 2, Oct. 1998, pp. 907–912.
[26] Y. Han, G. Cheung, A. Li, C. R. Sullivan, and D. J. Perreault, "Evaluation of magnetic materials for very high frequency power applications," in *Proc. IEEE Power Electron. Specialists Conf.*, Jun. 2008, pp. 4270–4276.
[27] C. P. Steinmetz, "On the law of hysteresis," *Proc. IEEE*, vol. 72, no. 2, pp. 197–221, Feb. 1984.
[28] K. Venkatachalam, C. R. Sullivan, T. Abdallah, and H. Tacca, "Accurate prediction of ferrite core loss with nonsinusoidal waveforms using only Steinmetz parameters," in *Proc. IEEE Workshop Comput. Power Electron.*, 2002, pp. 36–41.
[29] V. J. Thottuvelil, T. G. Wilson, and H. A. Owen, "High-frequency measurement techniques for magnetic cores," *IEEE Trans. Power Electron.*, vol. 5, no. 1, pp. 41–53, Jan. 1990.

Satyaki Mukherjee (Student Member, IEEE) received the B.Tech. and M.Tech. degrees in electrical engineering from the Indian Institute of Technology, Kharagpur, India, in 2017 and 2018, respectively. He is currently working toward the Ph.D. degree with the Colorado Power Electronics Center (CoPEC), University of Colorado, Boulder, USA.

He held a Graduate Student Intern position with Kilby Labs of Texas Instruments Inc., Santa Clara, USA, in 2019. His current research interests include power electronics for renewable energy sources, high-frequency power conversion using wide bandgap semiconductors, high-frequency magnetics design, automotive lighting, and digital control of switched-mode power converters.

Yucheng Gao (Student Member, IEEE) received the B.E. and M.S. degrees in electrical engineering from Tsinghua University, Beijing, China, in 2014 and 2016, respectively. He is currently working toward the Ph.D. degree with the Colorado Power Electronics Center (CoPEC), University of Colorado, Boulder, USA.

His current research interests include wide bandgap automotive power electronics, rectifier systems, and high-frequency magnetics design.

Dragan Maksimović (Fellow, IEEE) received the B.S. and M.S. degrees in electrical engineering from the University of Belgrade, Belgrade, Serbia, Yugoslavia, in 1984 and 1986, respectively, and the Ph.D. degree from the California Institute of Technology, Pasadena, CA, USA, in 1989.

From 1989 to 1992, he was with the University of Belgrade. Since 1992, he has been with the Department of Electrical, Computer and Energy Engineering, University of Colorado, Boulder, CO, USA, where he is currently a Professor and Co-Director of the Colorado Power Electronics Center. His current research interests include power electronics for renewable energy sources and energy efficiency, high-frequency power conversion using wide bandgap semiconductors, and digital control of switched-mode power converters. He has coauthored over 300 publications and the textbooks *Fundamentals of Power Electronics* (2nd edition, Springer 2001) and *Digital Control of High-Frequency Switched-Mode Power Converters* (Wiley-IEEE Press 2015).

Dr. Maksimović was the recipient of the 1997 NSF CAREER Award, the IEEE PELS Transactions Prize Paper Award in 1997, the IEEE PELS Prize Letter Awards in 2009 and 2010, the University of Colorado Inventor of the Year Award in 2006, the IEEE PELS Modeling and Control Technical Achievement Award for 2012, the Holland Excellence in Teaching Awards in 2004, 2011, and 2018, the Charles Hutchinson Memorial Teaching Award for 2012, and the 2013 Boulder Faculty Assembly Excellence in Teaching Award.